International Journal of Multiphase Flow 198 (2026) 105642

Contents lists available at ScienceDirect

International Journal of Multiphase Flow

journal homepage: www.elsevier.com/locate/ijmulflow

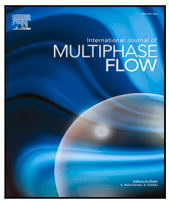

Research Paper

Uncovering Taylor bubble interfacial flow with high spatial resolution velocity measurement

Blaž Mikuž [a,*], Jan Kren [a], Mitja Uršič [a,b], Iztok Tiselj [a,b]

[a] Reactor Engineering Division, Jožef Stefan Institute, Jamova cesta 39, 1000 Ljubljana, Slovenia
[b] Faculty of Mathematics and Physics, University of Ljubljana, Jadranska 19, 1000 Ljubljana, Slovenia

ARTICLE INFO

Keywords:
Taylor bubble
Capillary waves
Vortex dynamics
Particle Tracking Velocimetry (PTV)
Dynamic masking

ABSTRACT

The dynamics of Taylor bubbles is investigated in a counter-current water flow, where the downward liquid flow in a vertical pipe counterbalances buoyancy, allowing extended steady-state observations. Using a combination of Particle Tracking Velocimetry (PTV), Laser-Induced Fluorescence (LIF), shadowgraphy, and dynamic masking, we unveil interfacial flow features, including tiny capillary waves. Velocity fields are measured for Taylor bubbles of varying lengths (1.2 D–14.9 D) in D=12.4 mm diameter pipe. Upstream of the bubbles, the liquid flow is laminar with $Re = 1270$ whereas the bubble behavior is characterized by $Eo = 21$ and $N_f = 4830$. In the liquid film region, the flow accelerates rapidly reaching up to about eight times the bulk velocity for the longest bubbles, yet no transition to turbulence is observed. The liquid film stabilizes at its final thickness and terminal velocity is reached for bubble lengths at about 5 D. Our measurements show that the bubble wake region hosts a strong primary toroidal vortex accompanied by a weaker, oppositely rotating secondary vortex. A particularly interesting is the emergence of stationary capillary waves at the bottom of the annular liquid film, likely associated to a localized widening of the liquid film region, reminiscent of a hydraulic jump where rapid flow abruptly decelerates. Velocity profiles, captured with a 20 μm spatial resolution, expose significant interfacial shear, observed exclusively downstream of the stationary capillary waves while remaining negligible elsewhere. This increased shear not only explains the observed phenomena but also suggests local flow motion within the gas bubble itself.

1. Introduction

Taylor bubble flow features elongated, bullet-shaped bubbles moving through pipes or channels, and separated by segments of liquid slugs. They have principal enabling role in many industrial applications, including steam generation in geothermal power plants, phase change processes in heat pumps and heat pipes, as well as advanced desalination technologies (Smith et al., 2002; Holagh and Ahmed, 2024). However, in some cases, Taylor bubbles are undesirable due to the high momentum of the liquid slugs. These slugs can exert significant forces on piping, potentially leading to structural damage, impaired thermal performance, or safety issues. Taylor bubbles exist in an extremely broad range of scales: from micrometers in microchannels of optofluidic applications (Bordbar et al., 2018; Čopar et al., 2020) to several dozen meters in strombolian volcanic eruptions and deep-water offshore drilling rigs (Zhou and Prosperetti, 2019). Their behavior is governed by gravitational, interfacial, viscous, and inertial forces, giving rise to a wide range of phenomena within the liquid and gas phases, as well as at the gas–liquid interface. However, non-intrusive experimental investigation of fluid velocity fields in such two-phase flows is challenging due to complex interfacial dynamics, including bubble deformation, tiny capillary waves, and interactions like coalescence and breakup.

First attempts to measure liquid velocity non-intrusively in two-phase flow focused on the bubbly flow regime (Hassan et al., 1992). Unlike single-phase flows, two-phase flows require distinguishing between gas and liquid phases, a challenge that drove the early development of phase separation methods (Deen et al., 2002; Khalitov and Longmire, 2002). According to Lindken and Merzkirch (2002), three common methods for phase separation were used at that time: Particle Image Velocimetry (PIV) with Laser Induced Fluorescence (LIF) (Sridhar and Katz, 1995), digital masking technique (Gui et al., 1997) and shadowgraphy (Nishino et al., 2000). Tokuhiro et al. (1998) combined PIV and shadowgraphy using two cameras, but angular discrepancies introduced errors due to the non-spherical shape of bubbles. Phase-separated velocity measurements using PIV with digital masking were

* Corresponding author.
E-mail address: blaz.mikuz@ijs.si (B. Mikuž).

https://doi.org/10.1016/j.ijmultiphaseflow.2026.105642
Received 9 July 2025; Received in revised form 18 January 2026; Accepted 1 February 2026
Available online 17 February 2026

first demonstrated in bubbly flows by Lindken et al. (1999) and Lindken and Merzkirch (2000). In their approach, the recorded images contained three gray level ranges: tracers (brightest), background illumination (medium), and bubble shadows (darkest), which allowed simultaneous extraction of PIV particle images and bubble contours from a single image. A significant achievement for the time was also the application of stereoscopic reconstruction of three-dimensional velocity vectors using multiple cameras (Hassan et al., 1998, 2001). An overview of different camera arrangements previously used in bubbly flow PIV imaging is provided by Sathe et al. (2010). They introduced a dichroic mirror to separate shadow and PIV images, which revealed slip velocity differences between single bubbles and bubble swarms. Planar fluorescence with rhodamine-B dye improves tracking of overlapping bubbles compared to shadowgraphy (Akhmetbekov et al., 2010). However, challenges persist; for example, even at low gas fractions in bubbly flows, interface reflections distort PIV/LIF measurements by illuminating particles outside the laser plane (Cerqueira et al., 2018), and accuracy is often reduced near phase boundaries in two-phase flows because interrogation windows contain information from both phases (Ergin et al., 2020). Thus, ongoing research continues to improve dynamic masks to better represent phase boundaries and reduce noise from reflections and shadows (Lemos et al., 2024). In the present study, a novel algorithm based on image intensity gradients (Kren et al., 2023) is applied to detect gas–liquid interfaces for dynamic masking of gas-phase regions.

In slug flows, Taylor bubbles are deformable, allowing capillary wave formation on the gas–liquid interface (Liberzon et al., 2006). The motion of Taylor bubbles has been extensively studied since the pioneering work of Dumitrescu (1943) and Davies and Taylor (1950), however the early experimental studies relied mainly on photographic images and theoretical calculations (Zukoski, 1966; Martin, 1976; Collins et al., 1978; Bendiksen, 1985; Campos and Carvalho, 1988). The first attempt to measure liquid velocity with PIV applied a solid mockup representing a Taylor bubble in a duct (Vassallo and Kumar, 1997). Polonsky et al. (1999) used PIV with fluorescent particles to measure the liquid flow ahead of a rising bubble. Additionally, higher velocities in the liquid film region were captured using the streak length method, where the length of particle streaks in each frame indicate liquid velocity. Van Hout et al. (2002) measured the complete velocity field around a 3.6 D-long Taylor bubble rising in a vertical pipe with a 25 mm inner diameter, analyzing radial and axial distributions of mean velocities and turbulence in bubble wake. Shemer et al. (2005) later extended this study to Taylor bubbles in laminar ($Re = 820$) and turbulent ($Re = 7500$) background flows. Subsequently, Shemer et al. (2007) investigated also rising Taylor bubbles in pipes with diameters ranging from 14 mm to 44 mm and Reynolds numbers up to 43 600, focusing on their influence on liquid flow and the transition from a toroidal wall jet to developed pipe flow. Bugg and Saad (2002) achieved a fairly good spatial resolution of 152 μm in PIV measurements of rising Taylor bubbles in stagnant olive oil and showed that the velocity profile in the lower portion of the liquid film fits the theoretical solution for a viscous falling liquid film very well. Pinto et al. (2005) used PIV to study Taylor bubble velocities in vertical co-current flow and found a bubble velocity transition at Reynolds numbers well below 2100. Nogueira et al. (2003) achieved improved spatial resolution of 70 μm while studying Taylor bubbles in aqueous glycerol solutions, analyzing both stagnant and co-current flow in a D = 32 mm vertical pipe. A key challenge identified was the "mirage effect", an optical distortion caused by light refraction at gas–liquid interfaces, compromising PIV accuracy in locating the precise interface. To mitigate this, shadowgraphy was integrated, using the method of Lindken and Merzkirch (2002), which combines PIV, LIF and pulsed shadowgraphy technique (PST). Velocity fields were measured at the bubble nose and in thin liquid film region (Nogueira et al., 2006a), as well as in the bubble wake (Nogueira et al., 2006b). These studies, performed over two decades ago, remain one of the best benchmark validation cases due to their spatial accuracy. More recently, Boucher et al. (2023) used PIV combined with shadowgraphy to investigate how Taylor bubble velocity depends on pipe inclination and liquid viscosity. The stagnation point location near the bubble nose and the interface curvature explained the reduced bubble velocity at low inclinations and high viscosity. Cerqueira et al. (2019) and Cerqueira and Paladino (2020) employed PIV/LIF with dynamic masking to investigate interactions between dispersed bubbles and Taylor bubbles in co-current turbulent flow, revealing a significant influence of the background gas volume fraction on the terminal velocity of Taylor bubbles. Similarly, gravity-driven slug flows were studied by Holagh and Ahmed (2025) also using the PIV/LIF technique; however, the liquid flow field was extracted using a robust image-processing approach involving adaptive thresholding and background subtraction. In both studies, relatively large interrogation windows were used, limiting the spatial resolution of the velocity fields measured by PIV method. Accurate velocity measurements of slug flow with higher spatial resolution are still needed, particularly for validating high-fidelity numerical simulations (Zimmer and Bolotnov, 2019; Frederix et al., 2020, 2023). To address this, the present study employs Particle Tracking Velocimetry (PTV), which, in contrast to PIV, tracks individual seeding particles and offers superior spatial resolution.

A comprehensive review of slug flow studies by Morgado et al. (2016) and Holagh and Ahmed (2024) shows that most research to date has focused on Taylor bubbles rising in either quiescent or co-current liquid flows. Substantial progress in understanding flow behavior has been achieved through the development of increasingly more accurate numerical methods featuring high spatial resolution and advanced interface reconstruction or sharpening techniques. These approaches have been applied to laminar co-current Taylor bubble flows in capillary channels (Ferrari et al., 2017; Magnini et al., 2017, 2019; Batchvarov et al., 2020; Magnini and Herrada, 2025), as well as to Taylor bubbles in the laminar–turbulent transition regime (Zimmer and Bolotnov, 2019, 2020, 2021) and in moderate turbulent flow conditions (Frederix et al., 2020, 2023). Taylor bubbles in counter-current flows attracted less attention, in particular in experimental studies (Benattalah et al., 2011). As a consequence, the existing models developed for vertical upward flow fail to predict correctly the slug void fraction in vertical downward flow (Saidj et al., 2025). In counter-current flow an interesting phenomena can be observed when Taylor bubble losses its axial symmetry and transitions into an asymmetric shape (Martin, 1976; Lu and Prosperetti, 2006; Fabre and Figueroa-Espinoza, 2014; Fershtman et al., 2017; Abubakar and Matar, 2022; Kren et al., 2023). The stability of Taylor bubbles in counter-current liquid flow was recently investigated numerically by Abubakar and Matar (2022), who found that it is strongly influenced by the bubble nose curvature and the Eötvös number ($Eo = \rho g D^2/\sigma$). At high Eo values, corresponding to weak surface tension effects, the instability manifests as deflections at the bubble's nose. Conversely, at low Eo values, where surface tension effects are strong, the instability appears as interface undulations (i.e. stationary capillary waves) at the bubble's tail due to interfacial stresses. Their study covered a range of $Eo = 20$–300, while the inverse viscosity number $N_f = (Eo^3/M)^{1/4}$, commonly used to characterize bubble wake dynamics, remained relatively low, i.e. $N_f < 300$.

In our present study, we experimentally investigate air–water Taylor bubbles exposed to counter-current flow in a vertical pipe. The liquid Reynolds number upstream the bubble is laminar with $Re = 1270$ and the obtained $Eo = 21$ results in a fully symmetric bubble nose of the Taylor bubble, well below the symmetry breaking. However, the inverse viscosity number reaches $N_f = 4830$, which is significantly higher than in the study by Abubakar and Matar (2022). At this elevated N_f, the flow exhibits both stationary capillary waves and unsteady flapping of the bubble's tail. Thus, this study investigates a compelling case of a Taylor bubble in counter-current flow, employing high-resolution velocity measurements of the liquid phase to gain deeper insight into the flow field, with a particular focus on the liquid film region and

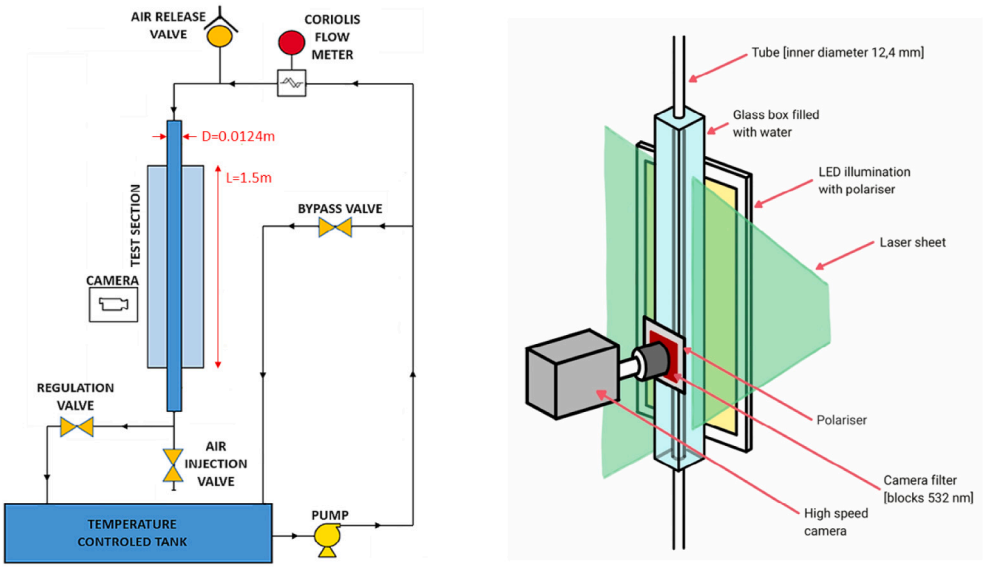

Fig. 1. Schematic of the experimental setup for investigation of Taylor bubbles in counter-current liquid flow (left) and schematic of the test section location with the high-speed camera position and illumination setup from LED and laser (right).

formation of stationary capillary waves. A better understanding of liquid film hydrodynamics is still needed (Morgado et al., 2016) and it requires the use of advanced, high-accuracy measurement techniques, which is addressed in this study.

2. Experimental method

2.1. Experimental facility

We studied Taylor bubbles in a counter-current flow conditions, where the buoyancy of the bubble is counterbalanced by the opposing water flow. Fig. 1 illustrates the experimental setup, which enabled fine control of bubble motion and maintained the Taylor bubble at a constant position for several hours. The facility consists of a transparent test section, pump, bypass valve, regulation valve, degassing valve, Coriolis flow meter, temperature sensors, pressure sensors and a water tank with thermal bath, which keeps a constant temperature during the long-term measurements. The test section is a straight pipe made of borosilicate glass with an inner diameter of 12.4 mm, pipe wall thickness of 1.8 mm and pipe length of 1.5 m. The pipe is surrounded by a glass box filled with water to reduce optical distortions of the images due to the light refraction at the boundaries between materials with different optical densities, e.g. water–glass interfaces. The gas bubble is injected into the pipe from a dead-end pipe at the bottom of the test section. Upstream of the test section, a flow homogenizer has been implemented to eliminate flow anisotropy downstream of the pipe bend. In order to achieve fully developed velocity profile, there is an additional distance of 80 D between the flow homogenizer and the camera recording location.

Camera recordings have been obtained using the LaVision PIV system composed of the Phantom v1212 high-speed camera and double cavity Litron Nd:YLF high-frequency pulsed laser. In all our experiments, the shape of the Taylor bubble nose is approximately symmetric and its position is centered at the pipe center-line (Nop et al., 2023; Tiselj et al., 2025). However, despite the laminar flow, the Taylor bubble axial position is slightly varying during the recordings. The memory of the high-speed camera allowed collection of up to 50,000 images. Camera recordings were performed using two lens configurations. The 100 mm lens provided a spatial resolution of approximately 14 pixel/mm, with images captured at a sampling frequency of 800 Hz. This setup allowed for recording durations of about 62 s in single-frame mode and 31 s in double-frame mode. For higher magnification, a 25 mm lens was used, yielding a spatial resolution of around 100 pixel/mm. These recordings were performed at a sampling frequency of 2 kHz, resulting in a maximum duration of approximately 12 s.

The measured flow parameters, including the flow rates, and their standard variations are given in Table 1. In order to check the reproductability, each test was repeated twice. It should be noted that the accuracy of the Coriolis flow meter is 0.1% of the measured value. Since this is an order of magnitude less than the standard variations measured during our tests (see Table 1), the flow measurement uncertainty can be attributed to the unsteadiness generated by the pump and the regulation valve. The regulation valve is used for fine flow adjustments during the tests to maintain the bubble at more or less constant position in the pipe. The water properties have been calculated from the NIST database (Lemmon et al., 2018).

2.2. Laser induced fluorescence

In two-phase flows, a significant challenge of the PIV method is the intense light reflection from the gas–liquid interface, which can damage the sensitive sensor of the high-speed camera. To prevent this, we combined PIV with Laser Induced Fluorescence (LIF) method, using special seeding particles that emit light at different wavelengths than the laser light. Specifically, we used polymethyl methacrylate (PMMA) particles coated with rhodamine B, which emit light in the orange-red spectrum of light, i.e. from 580 nm to 610 nm. Simultaneously, a special camera filter was used, which effectively blocks the light below 540 nm including the green laser light emitted at 527 nm. The applied PMMA particles are 20–50 μm in size with density of 1.19 g/cm^3, which makes these particles almost neutrally buoyant in water with Stokes number of up to 0.003. However, even with the PIV method combined with LIF, light reflections still occur. Namely, multiple images of the original particle are visible at the bubble interface or pipe walls — see Appendix A. While these images do not pose a risk to the camera sensor, they are undesirable in image post-processing as they introduce artifacts that can compromise the accuracy of the results. To address this, we developed a method, which masks out all regions not relevant to our analysis. Since our focus was on measuring the velocity field of the water flow, we specifically masked out the areas corresponding to the gas bubble and the glass pipe wall. Our method relies on accurate detection of the gas–liquid interface from the images, which requires

Table 1
Measured flow parameters, i.e. mass flow rate ϕ_m, temperature T, pressure p, together with calculated fluid properties, i.e. surface tension σ, dynamic viscosity μ, liquid water density ρ and Reynolds number Re_L).

	L/D	ϕ_m (kg/min)	T (°C)	p (bar)	σ (10^{-3} N/m)	μ (mPa s)	ρ (kg/m^3)	Re_L
Case 1	1.2	0.64 ± 0.01	28.0 ± 0.1	1.446 ± 0.006	71.5	0.832	996.3	1310
Case 2	3.1	0.64 ± 0.01	27.9 ± 0.1	1.278 ± 0.005	71.5	0.834	996.3	1310
Case 3	4.3	0.63 ± 0.01	27.8 ± 0.1	1.515 ± 0.006	71.5	0.836	996.3	1280
Case 4	7.7	0.63 ± 0.01	28.9 ± 0.1	1.256 ± 0.005	71.4	0.816	996.0	1320
Case 5	14.5	0.64 ± 0.01	25.8 ± 0.1	1.136 ± 0.004	71.8	0.874	996.8	1250
Case 6	14.9	0.62 ± 0.01	25.7 ± 0.1	1.535 ± 0.003	71.9	0.876	996.9	1220

a clear contrast between the gas and liquid phase. The best contrast at the gas–liquid interface is achieved when a pair of linear polarizers are applied, as shown in Fig. 1. One polarizer is used at the LED light source whereas the second polarizer is applied at the camera lens. The orientation of the second polarizer is adjusted to achieve optimal contrast at the gas–liquid interface. Since Taylor bubbles change shape over time, the method needs to detect the gas–liquid interface and reconstruct the bubble shape at each time step, which necessitates a dynamic masking approach. The best results were achieved when the measurements were conducted in pairs, using two sets of images: the first image in each pair was taken with laser illumination, while the second was captured immediately after the first one without the laser illumination, as shown in Fig. 2. The seeding particles are clearly visible only in the laser-illuminated images, whereas the second image in the pair provides optimal contrast at the gas–liquid interface, which is essential for generating dynamic masks. It is important to note that the time interval between the two images in each pair is short enough to ensure that the Taylor bubble does not change shape.

2.3. Dynamic masking

Our dynamic masking algorithm is derived from an algorithm, which has been initially developed for recognition of gas–liquid interface, described in details by Kren et al. (2023). This algorithm yields a high relative sensitivity of only one-fifth of an image pixel, enabling the tracking of tiny capillary waves traveling along the interface of a Taylor bubble. In the present analysis, the detection of edges (e.g. gas–liquid interfaces and the pipe's walls) has been improved with integrating noise removal and advanced edge detection techniques, which reduce the algorithm's sensitivity to variations in camera alignment and illumination between recordings. Noise is filtered out using anisotropic diffusion, i.e. the Perona–Malik filter, followed by edge detection with the Canny filter (Shih et al., 2009). Although this detection method can struggle with lower-quality or less sharp images, we address this by implementing a time-consuming step that connects detected edges in a close vicinity of the gas–liquid interfaces. We use the depth-first search algorithm to identify and connect these closely spaced edges. Once the gas–liquid interface is detected and the initial mask is created, subsequent images are analyzed based on the previous edge detection: since the bubble moves minimally between consecutive images, we only search for a new edges near the previously detected interface. This approach significantly accelerates the analysis and enhances the robustness of the code. In the final step, the algorithm aligns the images so that the vertical position of the Taylor bubble remains constant within the same recording. This is essential for obtaining sharp time-averaged results. The most suitable reference point in most recordings is position of the Taylor bubble nose, which is symmetric and moves only in the axial direction. However, for bubbles longer than 6 D and outside the camera's full field of view, image alignment was based on maintaining a constant visible bubble area across all frames. In the high-magnification recordings of the liquid film region, the images were aligned using the lowest stationary capillary wave as a reference point.

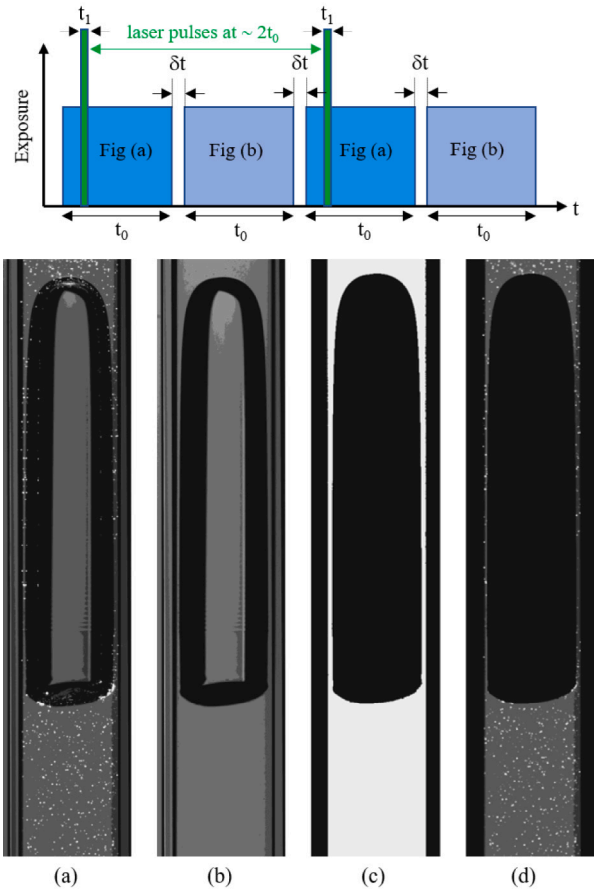

Fig. 2. PTV with dynamic masking: (a) raw PTV image with laser illumination of the seeding particles, (b) raw image with ambient illumination, (c) mask created from the second image and (d) mask merged with the PTV image. At a sampling frequency of 800 Hz, the camera exposure duration is $t_0 = 623.8$ μs, while the interval between sequential exposures, $\delta t = 1.2$ μs, and the laser pulse duration, $t_1 = 0.1$ μs, are significantly shorter.

2.4. Particle tracking velocimetry

Particle Tracking Velocimetry (PTV) tracks the motion of individual seeding particles, enabling high spatial resolution in flow measurements. This capability is particularly advantageous in the annular liquid film region of a Taylor bubble, where the liquid film is around half a millimeter thick. As a result, PTV provides detailed insights into the flow field with large velocity gradients within this thin region, bounded by pipe wall on one side and gas–liquid interface on the other side.

The PTV analysis was performed with the DaVis software version 10.2.1 (LaVision, 2024). For particle detection, we applied an intensity threshold above the image noise level and imposed an additional constraint on particle sizes, typically ranging from 3 to 6 pixels for low resolution recordings using 100 mm lens. The particle trajectories

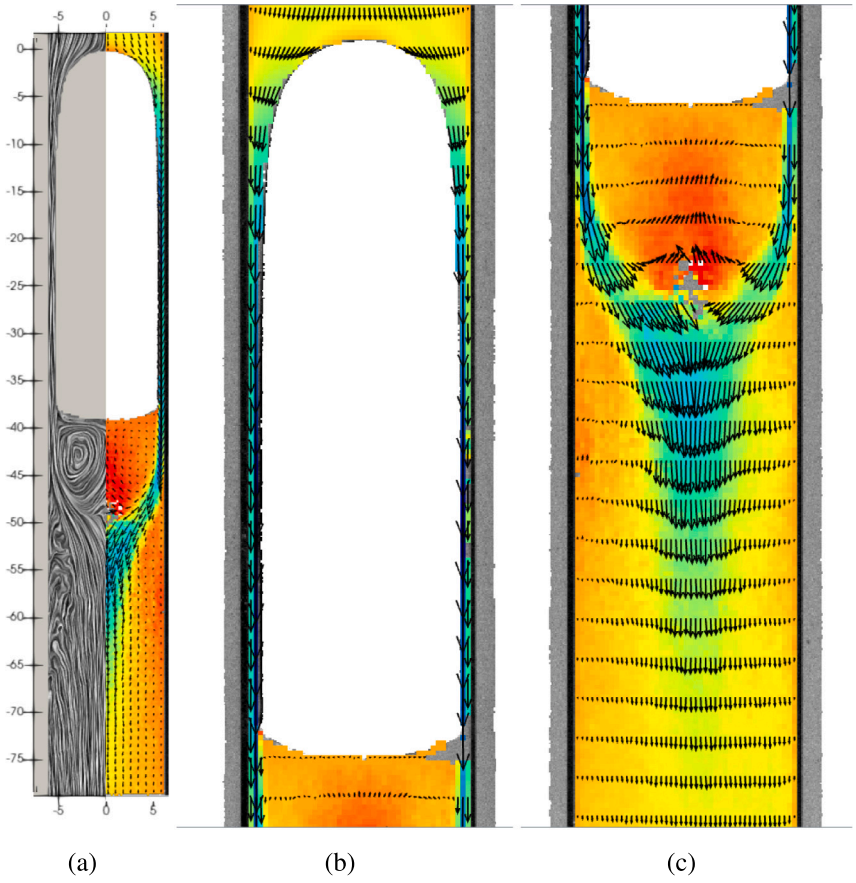

Fig. 3. Liquid velocity field surrounding a Taylor bubble in counter-current flow (Case 2 in Table 1): (a) overall view with streamlines on the left and vector field on the right side, (b) bubble nose and annular liquid film region, and (c) bubble wake region with strong primary and weak secondary toroidal vortices. The color field represents the streamwise velocity, with red and green–blue indicating upstream and downstream flow, respectively. The vector field is shown at reduced spatial resolution for better clarity. (For interpretation of the references to color in this figure legend, the reader is referred to the web version of this article.)

were then reconstructed with a minimum track length of 6 time steps, while acceleration constraints were used to limit the maximum absolute change in particle displacement of one pixel, or a maximum relative change in particle displacement of 20%. For high-magnification recordings, the apparent particle sizes ranged from 4 to 13 pixels, and the minimum track length was again set to six time steps. In this case, the maximum absolute and relative changes in particle displacement were limited to 20 pixels and 20%, respectively.

To obtain statistically meaningful velocity fields, the instantaneous Lagrangian particle trajectories were converted into a regular Eulerian velocity field using a Gaussian-weighted interpolation scheme, following the standard Eulerian–Lagrangian PTV processing approach. The resulting velocity fields were then ensemble-averaged over all recorded images during the steady-state period of the experiment to produce the time-averaged velocity fields presented in the next section. This averaging procedure effectively filters random noise and ensures that the reported velocity fields represent statistically converged mean flow quantities derived from several thousand individual particle trajectories.

3. Global velocity field measurements

Velocity measurements in this section were obtained using a 100 mm lens, providing a spatial resolution of 14 pixel/mm. The pipe diameter of 12.4 mm was used to scale pixel data into physical units.

3.1. Main flow characteristics

In Taylor bubble flows, the liquid flow field is typically divided into three regions: the bubble nose, the liquid film, and the bubble wake. Fig. 3 illustrates the key flow features measured for a Taylor bubble in a counter-current liquid flow. The upstream liquid redistributes evenly around the bubble nose and accelerates along the liquid film, which gradually thins toward the bubble tail. The upstream flow has been well characterized in prior measurements and analytical studies, therefore it is not discussed further here.

In the bubble wake, a strong primary vortex forms just behind the bubble, accompanied by a weaker secondary vortex further downstream and near the pipe wall, both indicated by the orange-red regions in the contour plots. Due to the axial symmetry of the pipe, both vortices are toroidal and are driven by the circumferential jet flow developed along the liquid film region of the Taylor bubble and detaching at the bubble's tail.

While the primary vortex has been widely investigated in terms of its size, shape, and intensity, the secondary vortex has received little attention in published studies. For counter-current Taylor bubble flow, the existence of the secondary vortex was first predicted in the high-fidelity simulations by Kren et al. (2024). Our present measurements confirm the presence of the secondary vortex, which rotates in the opposite direction with respect to the primary vortex. An indirect confirmation of the secondary vortex was recently reported also by Benattalah (2024), who measured wall shear stress along Taylor bubbles in a 10.2 mm pipe using an electrochemical double probe. Large voltage fluctuations indicated flow direction changes at wall, suggesting vortex

presence. The secondary vortex was estimated to be approximately 4 mm in length, with its position varying between 1.2 D and 2 D, shifting closer to the bubble's tail for shorter Taylor bubbles. A secondary vortex was previously observed also in rising Taylor bubbles in quiescent liquids (Van Hout et al., 2002; Cerqueira and Paladino, 2020). Van Hout et al. (2002) reported a weaker toroidal vortex with opposite rotation to the primary vortex, located 2 D–5 D downstream of the bubble's trailing edge.

The formation of the secondary vortex can be explained with an analogy with flow over a backward-facing step (BFS). Geometrically, the similarity lies in the expansion ratio E, defined in BFS as the ratio of step height to channel height, which is analogous to the ratio between Taylor bubble width and pipe diameter. Armaly et al. (1983) applied Laser Doppler Anemometry and showed that besides the primary re-circulating zone, which is attached to the BFS, additional regions of flow separation downstream of the step can be formed on both sides of the channel test section. The appearance of these secondary separation zones depend on both the expansion ratio E and the Reynolds number Re. It was shown that for $E = 0.5$, the second separation zone develops in the laminar range at about $Re = 400$ and remains in existence throughout the transition region up to turbulent regime, vanishing near $Re = 6600$ as the flow becomes fully turbulent. Thangam and Knight (1989) extended this analysis with numerical investigation of flow downstream BFS with varying E from 0.25 to 0.75 and found that increasing E leads to the added pressure rise along the channel causing the flow to decelerate along the upper wall and a deflection of the streamlines away from it. At high E, or Re, the flow can cause to separate along the upper wall, causing an additional displacement of the streamlines away from the wall, which suppress the size of primary vortex. Despite the rotational symmetry of our pipe, these findings align well with our flow conditions in the liquid film and bubble wake region of the Taylor bubble, with $Re = 1270$ placing the flow in the laminar-to-turbulent transition region, whereas the expansion ratio E is also quite large $E \approx (6.2\,\text{mm} - 0.5\,\text{mm})/6.2\,\text{mm} = 0.92$. Thus, the formation of the secondary vortex downstream the Taylor bubble can be attributed to the combined effects of free shear layer separation, pipe wall friction and an adverse pressure gradient caused by the expanding flow.

3.2. Influence of Taylor bubble length

We have analyzed liquid flow fields for Taylor bubbles of different lengths ranging from 1.2 D to 14.9 D, summarized in Table 1. Measured flow rates show that the upstream single-phase flow remains constant across all bubble lengths and is consistently laminar with a Reynolds number of 1270 ± 50.

The measured streamwise and spanwise velocity components for five different cases with varying lengths of the Taylor bubble are shown in Figs. 4 and 5. In cases 1–3, the Taylor bubbles are short enough to fit within the camera's field of view, while in cases 4 and 5, the bubbles are longer. For the latter, the focus is on the flow field at the bottom and downstream of the Taylor bubble. In all cases, the flow upstream the Taylor bubble is nearly axisymmetric. As the liquid reaches the bubble nose, a stable separation point forms at the tip of the bubble nose, causing the flow to distribute around the bubble into the surrounding liquid film region. The liquid film thickness gradually decreases, accelerating the liquid velocity within it. The longer the bubble, the larger the liquid velocity achieved in the liquid film. For the two longest bubbles (cases 4 and 5), we observed minor differences in liquid film thickness at opposite sides of the bubble, leading to differing velocities in these regions. Relatively large uncertainty of the liquid-film thickness measurements does not allow accurate identification of the (a)symmetries of the bubble. The PTV velocity measurements, on the other side, are more accurate and sensitive to much smaller asymmetries, thus the asymmetry effect becomes more clearly visible in the velocity field, in particular at the wake of the bubble. At the tail of the bubble, the toroidal liquid jet separates from the bubble, deflects inwards toward the center of the pipe and drives two counter-rotating toroidal vortices (dark blue color), i.e. the primary and secondary vortex as explained in Section 3.1 and shown in Fig. 3. The primary vortex is located just below the Taylor bubble, forming a bubble wake region, which is roughly one pipe diameter (D) in size for each case. For short bubbles (cases 1–3) the primary vortex is nearly axisymmetric, however, for longer bubbles the asymmetry of the liquid film induces asymmetry in the liquid flow field of the bubble wake region and further downstream.

The bubble wake region consistently exhibits asymmetry in every case. To verify repeatability, we conducted two measurements for each case, and the same asymmetry was always observed. The degree of asymmetry increases with the length of the Taylor bubble. Extended time averaging does not reduce this asymmetry, as the bubble's tail consistently shifts toward the same side in all cases. The possibility of upstream pipe bending affecting the results was ruled out through a numerical study by Mikuž et al. (2024), the use of a flow straightener located 90 D upstream of the test section and velocity analysis upstream the Taylor bubble for the Case 1 in Fig. 4. We also considered a possible pipe misalignment with the gravity direction, which was measured to be less than 2 mm over a length of 400 mm, corresponding to an angle of approximately 0.29 degrees. Additional tests performed with improved pipe alignment, reducing the estimated misalignment to below 0.03°, showed that the downstream flow remains asymmetric. Thus, the observed flow asymmetry is most likely associated with a weak instability of the bubble tail, which has been investigated numerically by Abubakar and Matar (2022) and experimentally by Tiselj et al. (2025).

3.3. Film thickness and terminal velocity

One of the key questions arising from our PTV measurements is whether the liquid film flow remains laminar or transitions to turbulence. As the film thins along the bubble's length, its velocity increases until the final thickness and a steady maximum velocity are achieved, known as terminal velocity. The terminal velocity represents a balance between gravity and viscous resistance and depends on film thickness and fluid properties. In laminar conditions, it can be predicted analytically using parabolic profiles, as shown in Appendix B. Eq. (B.6) provides an analytical expression for laminar film thickness, derived from the measured flow rate ϕ_m and fluid properties listed in Table 1, under the assumptions of axial symmetry and negligible interfacial shear stress τ. These assumptions lead to a uniform liquid film thickness along the pipe perimeter

$$h = \left(\frac{3\mu v_0 R}{2\rho g}\right)^{\frac{1}{3}} = \left(\frac{3\mu \phi_m}{2\pi R g \rho^2}\right)^{\frac{1}{3}} \approx 0.41\,\text{mm}. \quad (1)$$

The corresponding terminal interface velocity calculated from Eqs. (1) and (C.1) is 1.02 m/s, yielding liquid film Reynolds number $Re_F = v\rho h/\mu = 470$. While Nogueira et al. (2006a) reported a laminar–turbulent transition at $Re_F \approx 80$, Morgado et al. (2016) reported a broader transition range of $250 < Re_F < 800$, with the lower bound being less well defined. The minimum liquid film length required to reach terminal velocity is also uncertain. Nogueira et al. (2006a) observed liquid film development lengths of 2.2 D for Taylor bubbles in stagnant liquid and about 3.6 D in co-current flow, whereas in counter-current flow this has not been examined yet.

Table 2 summarizes the maximum film velocities measured by PTV for bubbles with L/D between 3.1 and 14.9. Terminal velocity appears to be reached between $L/D = 4.3$ and 7.7, which is significantly longer than in co-current or stagnant flows. This trend agrees with recent film thickness measurements by Tiselj et al. (2025), which showed that the film gradually thins and reaches its final thickness at a distance of approximately 5 D from the bubble nose.

We compared liquid film velocities from PTV measurements with velocities calculated from two additional methods, which are based on

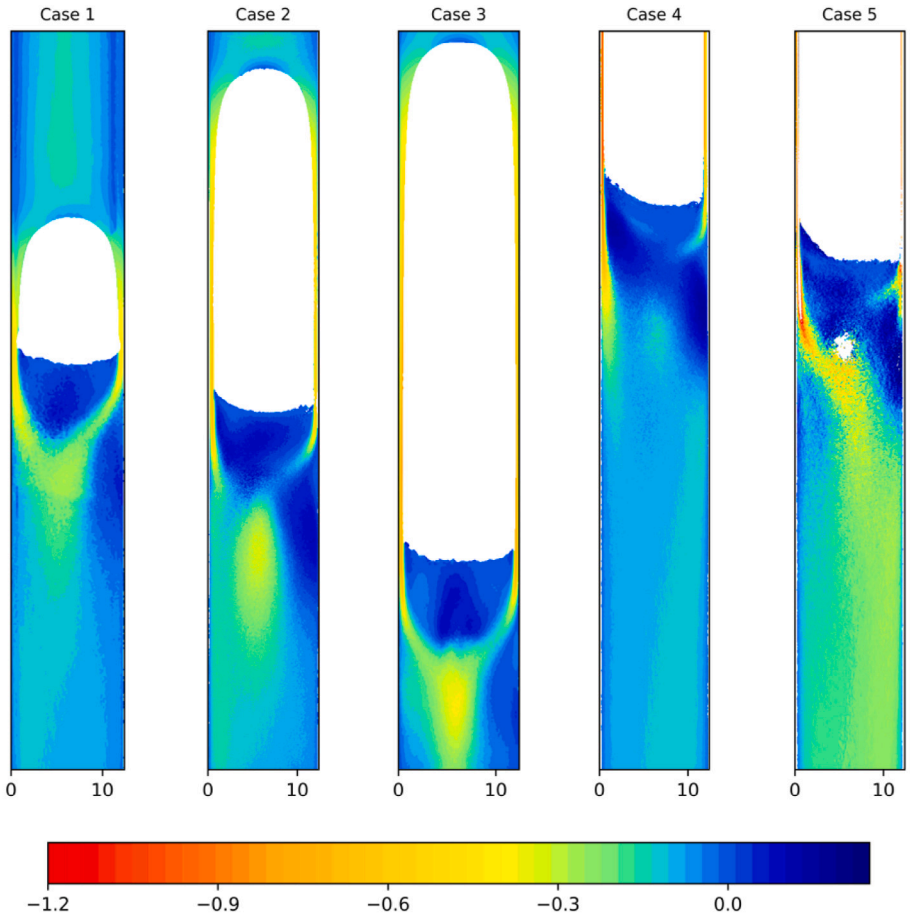

Fig. 4. Time-averaged streamwise velocity component for five cases with different lengths of Taylor bubbles: 1.2 D, 3.1 D, 4.3 D, 7.7 D and 14.9 D for Cases 1–5, respectively. The values in colormap have units of m/s. (For interpretation of the references to color in this figure legend, the reader is referred to the web version of this article.)

Table 2
Comparison of maximum liquid film velocities measured with different methods.

	L/D	From film thickness	From capillary waves		From PTV	
		v_i (m/s)	Thin film side c (m/s)	Thick film side c (m/s)	Thin film side v (m/s)	Thick film side v (m/s)
Case 2	3.1	0.7 ± 0.1	0.68 ± 0.05	0.68 ± 0.05	0.68 ± 0.02	0.62 ± 0.02
Case 3	4.3	0.9 ± 0.2	0.84 ± 0.05	0.84 ± 0.05	0.82 ± 0.02	0.82 ± 0.02
Case 4	7.7	1.2 ± 0.3	0.98 ± 0.05	0.89 ± 0.05	0.94 ± 0.02	0.78 ± 0.02
Case 5	14.5	1.1 ± 0.3	0.95 ± 0.05	0.85 ± 0.05	1.03 ± 0.02	0.70 ± 0.02
Case 6	14.9	1.3 ± 0.3	0.94 ± 0.05	0.83 ± 0.05	1.02 ± 0.02	0.79 ± 0.02

liquid film thickness and capillary wave wavelengths, as detailed in Appendix C. Among them, PTV consistently yields the most accurate results, followed by wavelength based velocities c, while estimates from liquid film thickness v_i carry higher uncertainty in the range of 15% to 25% due to the measurement error of liquid film thickness. For short bubbles $L/D \leq 4.3$, all three methods yield similar results. However, for long bubbles $L/D \geq 7.7$, asymmetry in film velocities is detected on opposite sides of Taylor bubbles. It is believed that this asymmetry is related to small differences in liquid film thicknesses: a thinner film side exhibits higher velocity and vice-versa. Notably, wave velocities c consistently fall within the range of measured PTV values, likely due to surface tension acting as a stabilizing link across the interface. In general, c agrees with PTV within 10%, whereas v_i tends to overestimate the velocity.

Although the terminal velocity and film development length have been determined, the flow regime remains unclear and is addressed in more detail in the following section.

4. High-resolution velocity measurements

We closely examined Taylor bubbles with length of $8.0\,D \pm 0.5\,D$, which is sufficiently long for the liquid film to reach terminal velocity. Particular attention was given to accurately aligning the vertical pipe with the gravity direction. Using a 2 m-long plumb line, we achieved a deviation of less than 0.03 degree, an order of magnitude smaller than in the previous section. Flow field at the bubble rear meniscus and in the liquid film has been investigated with large magnification using the 25 mm macro lens, which enabled us to achieve a spatial resolution of up to 100 pixels per millimeter. The scaling from pixels to physical units was performed using a separate image of a 0.6 mm thick wire inserted into the water-filled pipe. The high spatial resolution allowed us to identify regions with significant velocity gradients and investigate whether the flow in the liquid film region is laminar or turbulent. However, the high magnification restricted the camera's field of view to a short section of the bubble. Moreover, despite using a

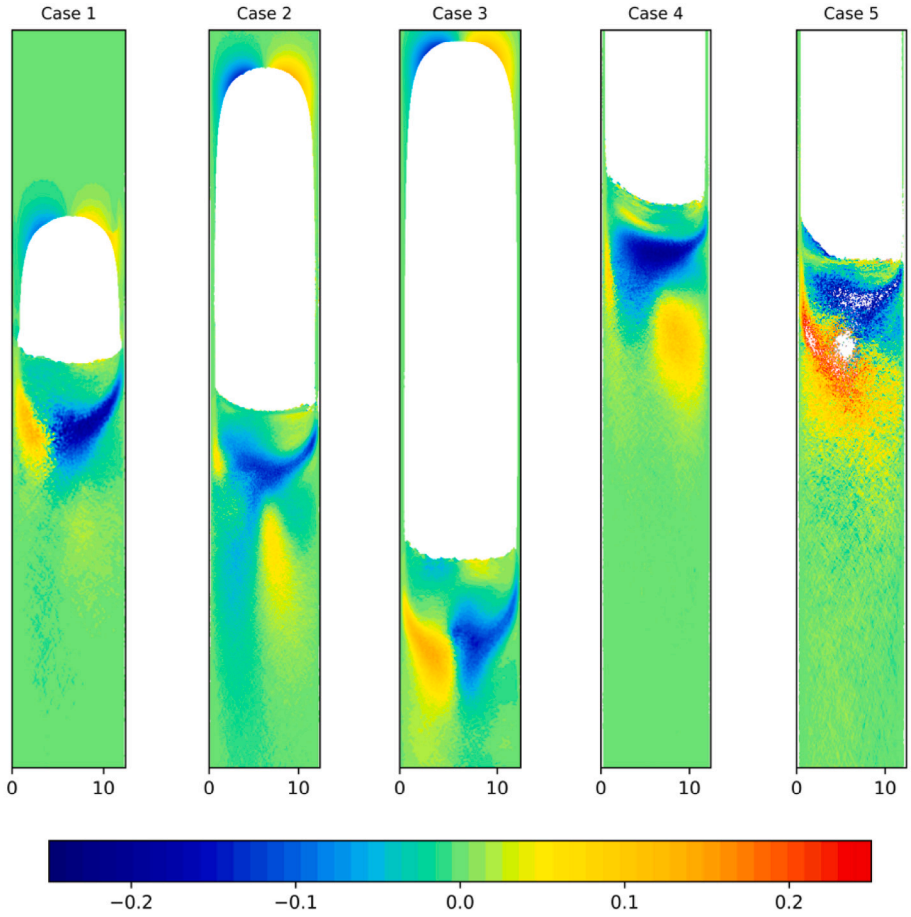

Fig. 5. Time-averaged radial velocity component for five cases with different lengths of Taylor bubbles: 1.2 D, 3.1 D, 4.3 D, 7.7 D and 14.9 D for Cases 1–5, respectively. The values in colormap have units of m/s. (For interpretation of the references to color in this figure legend, the reader is referred to the web version of this article.)

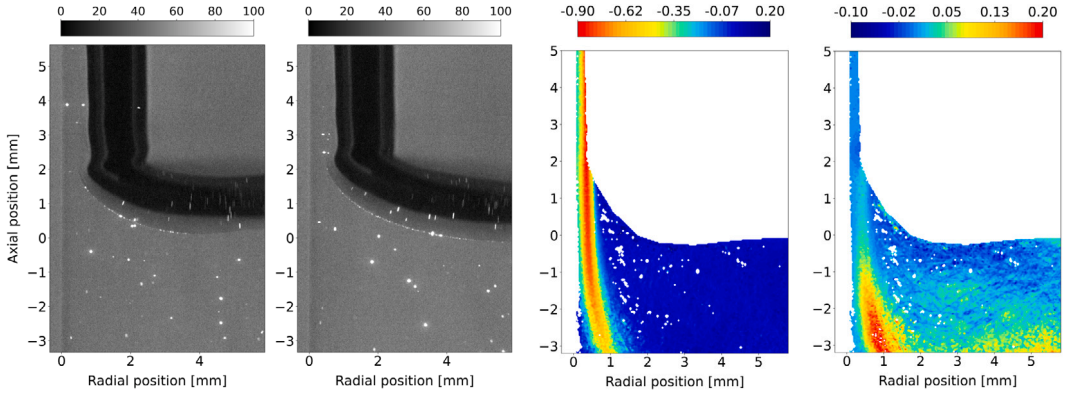

Fig. 6. Two raw images showing the trailing edge of the Taylor bubble at different time instances (a) and (b), and the measured time-averaged liquid velocity fields for the streamwise (c) and radial (d) velocity components. Pipe wall is located at the x-axis position of 0. (For interpretation of the references to color in this figure legend, the reader is referred to the web version of this article.)

water-filled glass box to reduce optical distortions, the interpretation of the magnified results inside a liquid film region is significantly more challenging, as emphasized in Appendix A.

4.1. Bubble rear meniscus region

Fig. 6 presents results for the bottom part of the Taylor bubble, where the liquid jet detaches from the bubble's interface. It should be noted that the bubble tail is indeed unstable in our case. The extent of this unsteady motion is illustrated in the two sample images shown in Fig. 6a and b. These images reveal also the difficulty of tracking the gas–liquid interface, which is not exactly at the location of the strongest contrast – similar to the issue observed in the liquid film recordings, which is explained in the following section. The streamwise velocity field U_s reveals the fastest liquid motion in the film region close to

the gas–liquid interface, remaining large as well in the jet flow as it separates from the trailing edge of the bubble. Contrarily, the slowest velocity is observed at the pipe walls and nearly zero velocity U_s is measured in the region about 2 mm downstream the bubbles' trailing edge. The measured radial velocity component U_r reveals an outward expansion of the liquid jet away from the pipe wall (red regions of U_r), while simultaneously showing an inward liquid motion from the pipe center region toward the wall (blue regions of U_r).

To date, the flow near the rear meniscus of Taylor bubbles has received considerably less attention than that at the front (Magnini et al., 2017). When the Reynolds number of the laminar liquid flow is sufficiently high, shadowgraphy images of the rear meniscus reveal the presence of stationary capillary waves, often referred to as ripples or undulations, even for Taylor bubbles in small capillary tubes (Khodaparast et al., 2015). These waves have been systematically studied through numerical simulations for Capillary numbers $Ca < 0.1$ and Reynolds numbers up to $Re = 1000$ (Magnini et al., 2017). Inertial effects become relevant when the Weber number $We = Ca \cdot Re$ exceeds 0.1, leading to a greater number of wave crests that are clearly visible on the rear interface of the bubble. At higher Reynolds numbers, these waves become unsteady, as reported by Ferrari et al. (2017). Buoyancy also plays a significant role, increasing the wave amplitude and reducing the wavelength (Magnini et al., 2019). It is important to emphasize, however, that all of these studies were conducted under co-current flow conditions, which differ significantly from the counter-current configuration considered in the present work. In addition, while numerical simulations of flow in narrow channels are typically validated using only shadowgraphy images, PTV measurements provide valuable supplementary information on the velocity field.

4.2. Liquid film region

The analysis of a liquid film region is focused on the region of stationary capillary waves, downstream which the liquid film thickness increases by approximately 10%. Stationary capillary waves (undulations) have been observed in both the experimental study of Benattalah et al. (2011), who examined Taylor bubbles in counter-current flow in a 10.2 mm pipe, and in our recent work by Tiselj et al. (2025) using a 12.4 mm pipe. The latter typically revealed 5–10 undulations, spanning one-fifth to one-third of the pipe diameter and located about 0.25D to 0.5D above the bubble tail, which is slightly lower than the 0.75D–0.9D range reported by Benattalah et al. (2011) for bubble lengths of 4.9D–7.8D.

Fig. 7 presents the results from the liquid film region at the location of stationary capillary waves. The pipe wall is located at the radial location of 0.0 mm, while the black area on the right corresponds to the gas–liquid interface. Due to light refraction, each seeding particle appears as a double image, as seen from the bright spots in Fig. 7a. The gas–liquid interface is also distorted by refraction; its corrected position, reconstructed from image analysis, is shown by the red line. The refraction effects in our optical system are detailed in Appendix A, and the velocity field was evaluated using only the seeding particles located to the left of the red line. Stationary capillary waves are visible in the center of the raw image, with the liquid jet flowing from top to bottom. The amplitude of the waves increases in the streamwise direction, with the lowest wave having the largest amplitude. This wave is chosen as a reference point for the axial position, with its position defined as zero. Upstream of the stationary capillary waves, the liquid film thickness is approximately 0.41 mm, while downstream it increases by about 10%. The high spatial resolution in our results reveals distinct differences in the velocity profile upstream and downstream of the stationary capillary waves. Upstream, the fastest velocity in the liquid film occurs precisely at the gas–liquid interface, whereas downstream, the highest velocity is found within the liquid film region, rather than at the interface. There are no significant flow features observed in the radial velocity component U_r. Fig. 7d shows the streamwise component of the Reynolds stress R_s, revealing laminar flow throughout the entire liquid film with no significant velocity fluctuations. An exception is observed downstream the stationary capillary waves, where an elevated values of Reynolds stress R_s indicate strong shear near the gas–liquid interface. This region is examined in more detail in the following two sections.

4.3. Effect of liquid impurities

Since water is a polar liquid, it is highly susceptible to contamination; therefore, it is important to verify that potential impurities or seeding particles do not alter the behavior of the pure Taylor bubble flow, particularly the capillary waves at the gas–liquid interface. Numerical simulations by Batchvarov et al. (2020) investigated the effect of surface-active agents (surfactants) on the tail and film dynamics of long Taylor bubbles propagating through capillary tubes in the visco-inertial regime. Variations in surfactant concentration along the gas–liquid interface induce surface tension gradients, i.e. so-called Marangoni stresses, which drive liquid away from regions with higher surfactant concentration. The study analyzed the influence of surfactant elasticity, bulk concentration, solubility, and diffusivity in the presence of inertial effects. It was found that surfactants significantly suppress tail undulations by accumulating near the trailing edge of the bubble, where strong Marangoni stresses locally rigidify the interface. At low surfactant solubility, the bubble shape exhibits two distinct regions: a surfactant-rich zone at the rear, and a surfactant-depleted region extending toward the bubble tip. Interestingly, the liquid film is thicker in the former and thinner in the latter, while two counter-rotating vortices within the bubble align precisely with the transition between these regions. These characteristic bubble shapes have been experimentally confirmed in square microchannels with width of 200 μm (Mori et al., 2024). Nevertheless, the findings of Batchvarov et al. (2020) are only partially relevant for our case, as their simulations pertain to a different flow configuration, which is co-current Taylor bubble flow, and operate at lower Reynolds numbers of up to Re = 728.

Unlike surfactants, seeding particles lack the amphiphilic structure, i.e. comprising hydrophilic and hydrophobic components that drives interface adsorption and reduces surface tension. Additionally, they are orders of magnitude larger than molecular-scale surfactants and are introduced at very low concentrations in PTV measurements, well below levels that could measurably alter interfacial behavior. Nevertheless, we observed seeding particle accumulation at the rear interface of Taylor bubbles, reminiscent of the interfacial stabilization seen in Pickering emulsions. To investigate whether this had any impact on the gas–liquid interface dynamics, we conducted comparative tests of Taylor bubbles in pure demineralized water (without seeding particles). We analyzed shadowgraphy images of interfacial waves (ripples), focusing on their wavelengths, which are closely linked to the interface velocity. As no significant differences were observed, we conclude that the seeding particles and other potential impurities present in our experiments do not affect the gas–liquid interfacial behavior. This insensitivity may be attributed to the relatively high Eötvös number ($Eo = 21$), indicating that surface tension effects are weak compared to gravitational and inertial forces.

In our recent study, Tiselj et al. (2025) analyzed the wavelengths of capillary waves ranging from 0.5 to 1.5 mm and found a strong correlation with the Taylor bubble length. This relationship arises from two main factors: (a) the capillary wave speed depends on its wavelength (see Eq. (C.2) in Appendix C), and (b) the liquid film velocity increases along the thinning film region. When the upward-propagating capillary waves reach a region where their propagation speed matches the oppositely directed local liquid velocity, they become trapped in a quasi-stationary position. It is interesting to note that Benattalah et al. (2011) reported wavelength of the observed stationary waves of about 1.24 mm, which corresponds to a somehow slower liquid film velocity than in our case. Nevertheless, this can be attributed to the shorter bubbles (5–8 cm) and smaller pipe diameter, i.e. 10.2 mm used in his experiments.

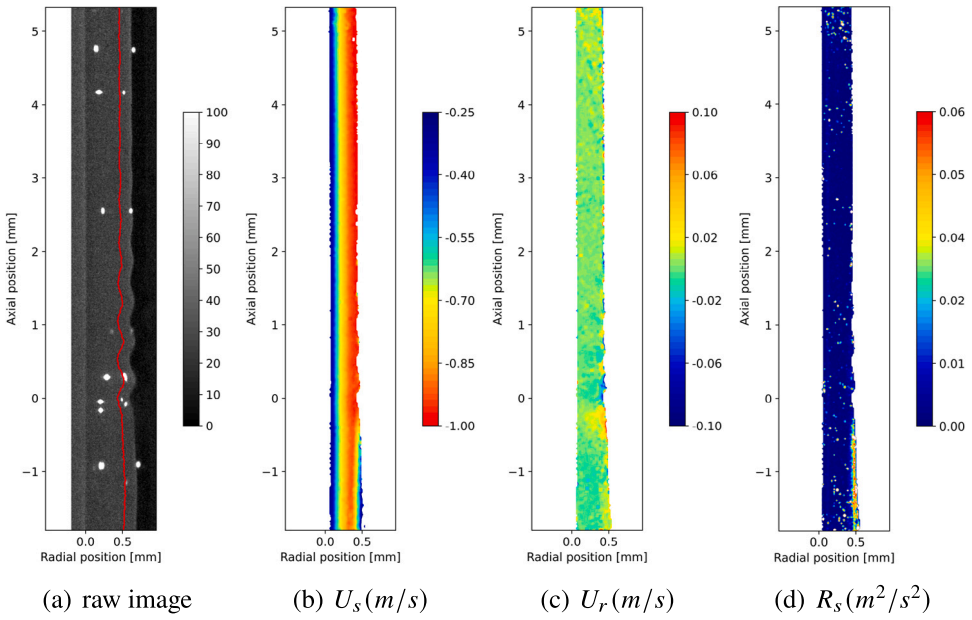

Fig. 7. Image of the liquid film region: (a) showing increased liquid film thickness downstream of axial position 0 mm, corresponding to the largest stationary wave amplitude. Due to light refraction each particle appears as two images; the pipe wall is at radial position 0, and the gas–liquid interface is marked by the red curve. Time-averaged fields within the liquid film: streamwise velocity (b), radial velocity (c), and streamwise Reynolds stress (d). (For interpretation of the references to color in this figure legend, the reader is referred to the web version of this article.)

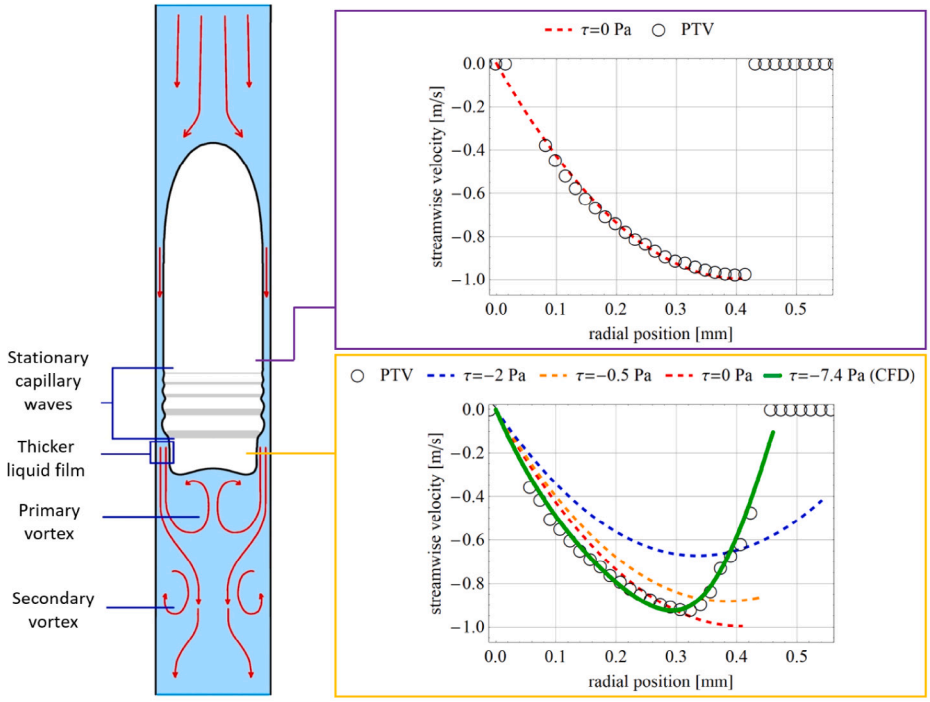

Fig. 8. Schematic of a Taylor bubble in a counter-current flow regime (left). Measured PTV velocity profile upstream (upper right) and downstream (bottom right) the stationary capillary waves. Analytical solutions for falling liquid film with different interfacial shear stresses are shown with dashed lines whereas the green line in the bottom graph corresponds to a numerical solution obtained with CFD simulation. (For interpretation of the references to color in this figure legend, the reader is referred to the web version of this article.)

4.4. Interfacial shear in liquid film region

The schematic in Fig. 8 illustrates the key features of a Taylor bubble in counter-current water flow, as identified from our present PTV measurements and analysis. These include laminar flow in the bubble nose and liquid film regions, stationary capillary waves, a liquid film widening region, a strong primary vortex, and a weaker secondary vortex in the bubble wake region. The widening of the annular liquid film region resembles a hydraulic jump, which is typically characterized by an abrupt transition from supercritical to subcritical flow due to a rapid deceleration of the liquid. Hydraulic jumps are usually driven by Froude number changes rather than a direct transition from

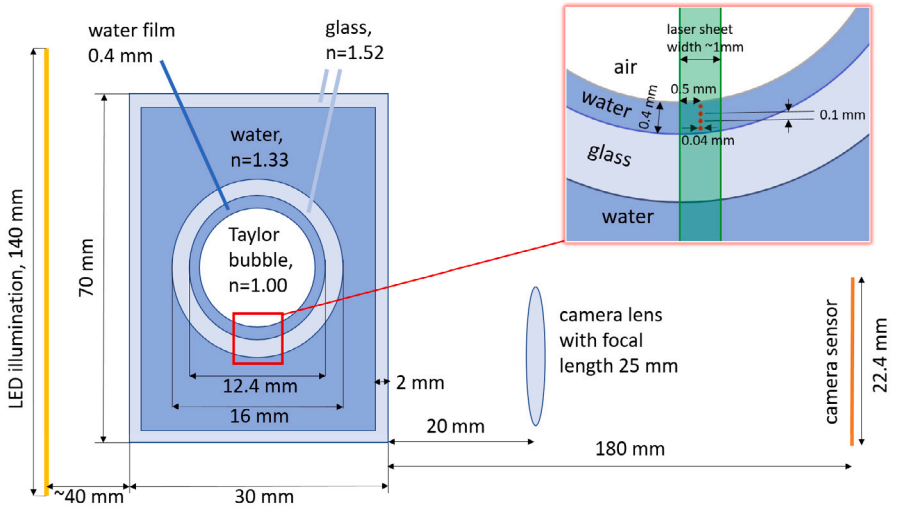

Fig. A.9. Top-view sketch of the simulated optical setup: a test section with a Taylor bubble inside a pipe, enclosed in a water-filled glass box. Refraction is modeled for light emitted by background LED illumination (yellow) and four laser-excited fluorescent seeding particles — see red dots in the zoomed-in image at the right top side. Images are captured by a high-speed camera with a 25 mm lens and finite sensor size. Lengths are not in scale. (For interpretation of the references to color in this figure legend, the reader is referred to the web version of this article.)

laminar to turbulent flow, which does not appear to be the case here, as the liquid film remains laminar throughout. Instead, we believe that the formation of stationary capillary waves is closely linked to the observed liquid film widening via interfacial shear stress, which we have examined in greater detail here.

In the literature, scarce data is found on the wall shear stress in the annular liquid film, primarily due to the inherent difficulties in performing experimental measurements in such thin flow region (Morgado et al., 2016; Benattalah, 2024). Data on interfacial shear stress are even scarcer; however, it is widely accepted that in Taylor bubble or slug flow, interfacial shear is either negligible or significantly lower than wall shear stress (Wallis, 1969; Nogueira et al., 2003, 2006a). When the interfacial shear stress is indeed negligible it is a common practice to apply models for freely falling liquid film. The simplified analytical solution for a laminar falling liquid film in two-dimensional flow is derived in Appendix B and demonstrates that both the liquid film thickness and velocity profile are sensitive to the shear stress at the gas–liquid interface. Specifically, if zero interfacial shear stress is assumed, the velocity reaches its maximum at the interface. However, when interfacial shear acts to drag the liquid, it leads to a thicker liquid film and reduced flow velocity.

Velocity profiles upstream and downstream of the stationary capillary waves have been extracted from the results in Fig. 7b. Although the concentration of the seeding particles on individual image in Fig. 7 may seem low, the average number of particles at each radial location in our statistical analysis is about 2000. Comparison of the profiles in the upper and bottom graphs in Fig. 8 reveals two key observations: (a) the liquid film region becomes 10% thicker downstream of the bottom-most wave, and (b) the maximum velocity position shifts inward from the gas–liquid interface into the liquid film region. In the near-wall region, within about 80 μm from the wall, the flow is slower, statistical accumulation is lower due to the limited recording times, and the measurements are also more susceptible to the optical distortions. Thus, these values have greater uncertainty and are excluded from the graphs.

The dashed lines in both graphs of Fig. 8 are analytical solutions of Eq. (B.2), assuming different shear stress values at the gas–liquid interface: 0 Pa, −0.5 Pa, and −2 Pa. The comparison between the analytical solutions and the measured values indicates nearly negligible interfacial shear for locations above the stationary capillary waves. In contrast, when a nonzero interfacial shear stress of −0.5 Pa or −2 Pa is assumed, the velocity profile deviates significantly from the measured PTV data due to the resulting increase in liquid film thickness. Note that the analytical solutions are inherently symmetric about their extrema due to their parabolic form.

Below the stationary capillary waves, the measured interfacial shear becomes significant and the measured PTV velocity profile is asymmetric, as shown in Fig. 8. This behavior is better understood by considering both the liquid film widening (expansion) and non-zero interfacial stress, as demonstrated by our simplified CFD model in Appendix D. The simulated velocity profile shows good agreement with the PTV measurements downstream of the stationary capillary waves when the interfacial shear stress is set to $\tau = 7.4$ Pa. For reference, this value is higher than the corresponding wall shear stress, $\tau_W = 5.0$ Pa, for the same velocity profile. These results suggest that stationary capillary waves and liquid film widening arise from significant shear near the bottom of the Taylor bubble. This shear likely results from opposing gas motion within the bubble, indicating that gas upstream and downstream of the stationary waves moves in opposite directions. The existence of such gas rotation inside the Taylor bubble was reported by Benattalah et al. (2011), however their vortex lacked axisymmetry and did not exhibit a toroidal structure. A toroidal vortex was numerically predicted by Kren et al. (2024) and further postulated by Tiselj et al. (2025) to explain the formation of stationary capillary waves.

5. Conclusions

In this study, we developed a novel velocity measurement technique for two-phase flows, which overcomes key challenges in gas–liquid flow visualization. The main obstacles for non-intrusive PTV in gas–liquid flows stem from scattered light, light refraction, reflections and optical distortions due to the gas–liquid interfaces. To mitigate these issues, we implemented PTV with LIF combined with a dynamic masking technique, effectively eliminating unwanted optical phenomena. Our measurements of the velocity fields achieve a spatial resolution of approximately 0.12 mm with the 100 mm lens and a remarkable resolution of 20 μm using the 25 mm macro lens.

Our method was applied to investigate the liquid flow dynamics surrounding Taylor bubbles in a counter-current water flow, where buoyancy-balanced bubbles ranged in length from 1.2 D to 14.9 D in a D = 12.4 mm pipe. The liquid flow rates required for balance correspond to Reynolds numbers of 1270 ± 50, independent of bubble length but

varying slightly with temperature and pressure. Velocity measurements revealed a laminar upstream flow, a liquid film accelerating up to eight times the bulk velocity for long enough bubbles, a strong primary vortex, and a weak secondary vortex in the bubble wake. The liquid film region was analyzed using three distinct methods, all of which indicate that liquid film acceleration ceases and terminal velocity is reached when the bubble length is about 5 D, significantly longer than in previously studied rising or co-current Taylor bubble flows. One of the research questions was whether the thin liquid film region surrounding the Taylor bubble becomes turbulent. Our high-resolution PTV measurements confirmed that the liquid film remains laminar for all bubble lengths, despite increased asymmetry downstream the Taylor bubble for longer bubbles. The flow asymmetry cannot be conclusively attributed to slight pipe misalignment with gravity nor to upstream flow conditions, however it can be instead attributed to a weak instability of the bubble tail, as reported by Abubakar and Matar (2022) and Tiselj et al. (2025).

Special attention was given to the thin liquid film above the bubble tail, where stationary capillary waves persist at the gas–liquid interface. In this region, the liquid film measures about 0.41 mm, but undergoes a 10% widening downstream the stationary capillary waves, resembling a hydraulic jump. High-resolution PTV velocity profiles revealed a laminar liquid film flow, even in this transition zone. Notably, in the thicker liquid film region, the velocity maximum shifts away from the gas–liquid interface, suggesting increased shear stress at the interface. This shear indicates that in the thicker liquid film region, the gas phase may move at a significantly different velocity, that is opposing the liquid flow.

Despite advancements, state-of-the-art numerical simulations still struggle to predict the formation of stationary capillary waves and the observed liquid film widening region. Therefore, the present study provides a valuable validation case for improving high-fidelity numerical simulations.

CRediT authorship contribution statement

Blaž Mikuž: Writing – original draft, Validation, Methodology, Investigation, Formal analysis, Data curation, Conceptualization. **Jan Kren:** Writing – review & editing, Visualization, Validation, Software, Methodology, Investigation, Formal analysis, Data curation. **Mitja Uršič:** Writing – review & editing, Methodology, Investigation, Funding acquisition, Formal analysis. **Iztok Tiselj:** Writing – review & editing, Supervision, Resources, Project administration, Investigation, Funding acquisition, Conceptualization.

Funding

The authors acknowledge the financial support from the Slovenian Research Agency [grant numbers P2-0026, NC-0026, V2-2375] and the Slovenian Nuclear Safety Administration [grant number V2-2375].

Declaration of competing interest

The authors declare that they have no known competing financial interests or personal relationships that could have appeared to influence the work reported in this paper.

Acknowledgments

The authors gratefully acknowledge our collegues and students for valuable contributions during their hands-on training in laboratory research: Peter Tiselj for preparation of the dynamic masks, Žiga Perne and Deja Razpet for measuring assistance, Paula Pérez Domínguez for assistance with plotting the results and Jakob Jakše for illustrating drawings in Figs. 1 and 8.

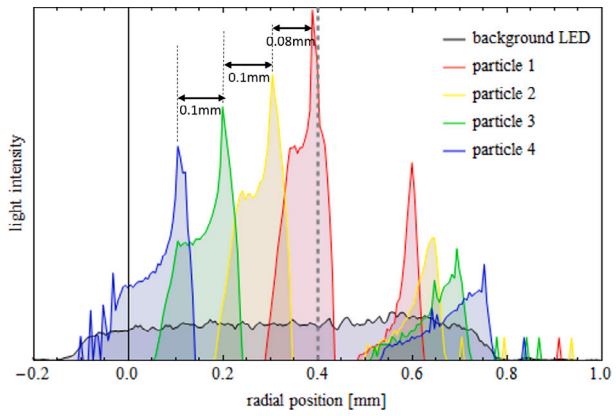

Fig. A.10. Simulated light refraction produces two distinct images for each of the four seeding particles, i.e. red, yellow, green, and blue curves. The image of liquid film illuminated by background LED (black curve), appears optically thicker than it actually is. Solid and dashed vertical lines mark the estimated location of the pipe wall and gas–liquid interface, respectively. (For interpretation of the references to color in this figure legend, the reader is referred to the web version of this article.)

Appendix A. Light refraction in a thin liquid film

Separate ray optics simulations were performed for measurements with the 100 mm and 25 mm camera lenses. The corrections of PIV images taken with 100 mm lens are similar to the corrections described in our recent paper by Tiselj et al. (2025). These corrections were obtained with the Ray Optics Simulation open-source software (Tu et al., 2016) and have a relevant influence on the measured liquid film thickness: liquid film thickness measured directly from the photographs without corrections for optical distortions, is around 20% thicker than the real liquid film inside the pipe.

Optical distortions specific for the present work are observed in images taken with the 25 mm lens. These distortions are more problematic, highly sensitive to slight changes in illumination and camera positioning, and require careful attention. Our 2D optical system used in ray optics simulations is shown in Fig. A.9. The setup includes a test section, illumination plane, lens, detector, and four small light sources representing PIV particles (red dots) located in the central plane of the laser sheet (green area). These particles have a finite size with diameter of 40 μm. Results of the simulations are shown in Fig. A.10 where one can see that length scale derived from the liquid film thickness cannot be used in analysis of radial locations of PIV particles. Each of the four PIV particles, separated for a specified distance within the liquid film (see upper right image in Fig. A.9), produces two images at the camera sensor. This effect results from two distinct optical paths between the light source and camera: most light refracts through the liquid film, glass and surrounding water, while some passes through the air bubble. Optical simulations confirm that particle duplication in Fig. A.9 disappears when the bubble is modeled as opaque. It also results in a thinner liquid film, supporting the reasoning behind the translation of the water–air interface shown in Fig. 7a.

Appendix B. Analytical solution for a falling liquid film

Flow in liquid film region of a Taylor bubble can be better understood with the theory of a falling liquid film, which was introduced by Nusselt (1916). It describes the development of a velocity profile in liquid films, which are balanced with gravitational forces, viscous forces, and sometimes surface tension effects. For steady-state laminar flow the governing equation for velocity $\vec{u}$ can simply be written as

$$\mu\nabla^2\vec{u} = \rho\vec{g}, \tag{B.1}$$

where ρ is liquid density and $\vec{g}$ gravity acceleration. Due to the relatively small liquid film thickness $h \ll 2R$, the wall can be approximated as planar, and Eq. (B.1) can be simplified to

$$\mu \frac{d^2u}{dy^2} = \rho g, \tag{B.2}$$

where y is wall-normal coordinate. The boundary conditions for the velocity u are the usual no-slip velocity condition at the wall and the (unknown) interfacial shear τ at the gas–liquid interface, i.e.

$$u(y=0) = 0, \qquad \frac{du}{dy}(y=h) = \frac{\tau}{\mu}. \tag{B.3}$$

Solution of Eq. (B.2) is a parabolic velocity profile

$$u(y) = \frac{\rho g}{\mu}\left(hy - \frac{y^2}{2}\right) + \frac{\tau}{\mu}y. \tag{B.4}$$

Clearly, from this velocity profile one can express the interface velocity $u(h)$ as well as derive the mean velocity in the liquid film region $\bar{u}$ as

$$u(h) = \frac{\rho g}{2\mu}h^2 + \frac{\tau}{\mu}h, \qquad \bar{u} = \frac{\rho g}{3\mu}h^2 + \frac{\tau}{2\mu}h. \tag{B.5}$$

Generally, the liquid film thickness h is unknown, however, it can be derived from the continuity equation when the liquid flow rate and interfacial shear stress τ are known. For example, in our Taylor bubble case, the liquid flow rate in the liquid film region equals the upstream single-phase liquid with bulk velocity v_0 and flow rate ϕ_m (given in Table 1), as dictated by the mass conservation. Assuming a uniform liquid film thickness h along the pipe perimeter of $2\pi R$, one can derive the h from a third order polynomial, i.e.

$$\frac{2\rho g}{3\mu}h^3 + \frac{\tau}{\mu}h^2 - v_0 R = 0. \tag{B.6}$$

This equation relates the liquid film thickness h to the interfacial shear stress τ: h is thinnest for large positive τ (same direction) and thickest for large negative τ (opposite direction). Eqs. (B.5) and (B.6) can be used to estimate the interfacial shear stress τ.

Brown (1965) derived the velocity profile and liquid film thickness for an annular liquid film assuming zero shear stress at the gas–liquid interface. For cases with non-zero interfacial shear, the solution follows from Eq. (B.1) in cylindrical coordinates, yielding an implicit equation for the liquid film thickness h, which is rather long and requires an iterative solving procedure. The annular geometry introduces only a minor correction, adjusting the factor in Eq. (C.1) from 1.5 to 1.517, thus, it is not discussed further here and is left to the reader.

Appendix C. Estimation of liquid film velocity

Maximum liquid film velocity can be estimated from the liquid film thickness h, as explained by Kren et al. (2023). This approach assumes that the liquid flow redistributes uniformly along the entire cross-sectional perimeter of the Taylor bubble, enabling us to derive the following expression for the liquid–air interface velocity:

$$v_i = 1.5\frac{v_0 R^2}{2Rh - h^2}, \tag{C.1}$$

where R is pipe radius. Coefficient 1.5 is introduced as a ratio between the maximum and the bulk velocity in the liquid film, which can be analytically derived from parabolic velocity profile of a laminar liquid film.

Another method for estimating the liquid film velocity analyzes the wavelengths λ of the observed stationary capillary waves, which depend on liquid velocity at the gas–liquid interface (Tiselj et al., 2025). In this method, the expression for phase velocity of the capillary waves stands:

$$c = \sqrt{\frac{\sigma}{\rho}\frac{2\pi}{\lambda}}, \tag{C.2}$$

where σ represents the surface tension and ρ liquid density of water. The primary uncertainty in the calculated liquid film velocity arises from the measurement uncertainty of the wavelength λ, which remains relatively low, i.e. $dc/c \sim 0.5 d\lambda/\lambda$.

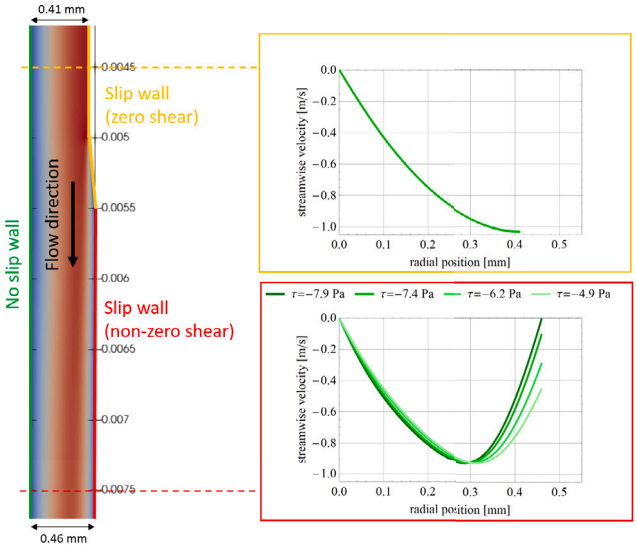

Fig. D.11. A simplified CFD geometry of the liquid film region with expansion between the axial locations of 0.005 m and 0.0055 m. The graphs on the right show the calculated streamwise velocity profiles within the liquid film region at two axial positions, i.e. upstream and downstream the expansion. Velocity profiles are calculated for different shear stress values applied at the slip wall boundary downstream of the expansion. Axial dimensions are presented in meters. (For interpretation of the references to color in this figure legend, the reader is referred to the web version of this article.)

Appendix D. Numerical model of a thin liquid film

Our flow conditions were investigated numerically with Computational Fluid Dynamics (CFD) by Nop et al. (2023) and Tiselj et al. (2024) using Direct Numerical Simulation (DNS) with the Front-Tracking method, and by Kren et al. (2024) and Kren (2024), using a high-resolution Large Eddy Simulation (LES) approach with the volume-of-fluid (VoF) and geometric interface capturing (PLIC) method. Both simulations predicted a symmetric shape of the bubble nose and unstable undulations of the tail with no significant bubble breakup at the bubble's tail. Interestingly, the LES was sufficient to gather ample statistics for capturing the weak secondary vortex in the bubble wake region, which has been now confirmed also with the present PTV measurements in Section 3. However, accurately predicting the tiny stationary capillary waves as well as the liquid film widening region remains a challenge and requires further refinement with more precise computational approaches.

The flow behavior downstream of the stationary capillary waves in the thin liquid film can be better understood using a simplified model of a liquid film flow in an expanding channel with variable interfacial shear, as shown in Fig. D.11. The dimensions of the two-dimensional channel are based on observations from recordings captured with the 25 mm macro lens: the upstream and downstream channel widths are 0.41 mm and 0.46 mm, respectively. A uniform inlet velocity of $v = v_0 R^2/(2Rh - h^2) = 0.68$ m/s is imposed at the channel entrance, assuming liquid film width $h = 0.41$ mm and mean velocity upstream the Taylor bubble $v_0 = \phi_m/(\rho\pi R^2) = 0.087$ m/s calculated from measured flow rates in Table 1. To ensure fully developed laminar flow before the expansion, the upstream length of the channel is set to 95 mm. This length matches that of the experimental Taylor bubble, which was sufficient to reach terminal velocity in the liquid film. The downstream section in our CFD model extends 5 mm beyond the expansion, which is sufficient to capture the post-expansion flow behavior. The left boundary of the domain (indicated by the green line in the left side of Fig. D.11) represents the pipe wall, where a no-slip boundary condition is

imposed. The right side of the computational domain corresponds to the gas–liquid interface, modeled using two different boundary conditions. Namely, to prevent excessive flow separation at the location of the lowermost stationary wave, the channel expansion is applied gradually between $x = 5$ mm and $x = 5.5$ mm, as shown in Fig. D.11. Upstream of $x = 5.5$ mm (indicated by the orange line), a slip boundary condition is applied on the right boundary, mimicking the typical zero-shear stress at a gas–liquid interface. That corresponds to the maximum liquid velocity at that boundary, as shown in the upper right graph of Fig. D.11. Downstream the expansion location (marked by the thick red line), a slip wall with non-zero shear stress was applied to simulate strong interfacial shear. Different values of interfacial shear stress are tested, which result in different velocity profiles as shown in bottom right graph of Fig. D.11.

Our CFD simulations demonstrate that the combined effect of the gradual expansion and the strong interfacial shear downstream can lead to an asymmetric velocity profile in the laminar liquid film, which cannot be captured by the analytical solutions presented in Appendix B. Furthermore, the simulations also reveal that the laminar liquid film remains stable, with no flow unsteadiness induced by the upstream channel expansion.

Appendix E. Supplementary data

Supplementary material related to this article can be found online at https://doi.org/10.1016/j.ijmultiphaseflow.2026.105642.

Data availability

Data will be made available on request.

References

Abubakar, H., Matar, O., 2022. Linear stability analysis of Taylor bubble motion in downward flowing liquids in vertical tubes. J. Fluid Mech. 941, A2.

Akhmetbekov, Y., Alekseenko, S., Dulin, V., Markovich, D., Pervunin, K., 2010. Planar fluorescence for round bubble imaging and its application for the study of an axisymmetric two-phase jet. Exp. Fluids 48, 615–629.

Armaly, B.F., Durst, F., Pereira, J.C.F., Schönung, B., 1983. Experimental and theoretical investigation of backward-facing step flow. J. Fluid Mech. 127, 473–496.

Batchvarov, A., Kahouadji, L., Magnini, M., Constante-Amores, C.R., Shin, S., Chergui, J., Juric, D., Craster, R.V., Matar, O.K., 2020. Effect of surfactant on elongated bubbles in capillary tubes at high Reynolds number. Phys. Rev. Fluids 5, 093605.

Benattalah, S., 2024. Experimental study of Dumitrescu–Taylor bubble wall shear stress in stagnant and counter-current vertical flow. Thermophys. Aeromech. 31, 865–877.

Benattalah, S., Aloui, F., Souhar, M., 2011. Experimental analysis on the counter-current Dumitrescu-Taylor bubble flow in a smooth vertical conduct of small diameter. J. Appl. Fluid Mech. 4 (4), 1–14.

Bendiksen, K.H., 1985. On the motion of long bubbles in vertical tubes. Int. J. Multiph. Flow 11 (6), 797–812.

Bordbar, A., Taassob, A., Zarnaghsh, A., Kamali, R., 2018. Slug flow in microchannels: Numerical simulation and applications. J. Ind. Eng. Chem. 62, 26–39.

Boucher, A., Karp, J., Belt, R., Liné, A., 2023. Dynamics of elongated bubbles in slightly inclined pipes with viscous fluids. J. Fluid Mech. 977.

Brown, R., 1965. The mechanics of large gas bubbles in tubes: I. Bubble velocities in stagnant liquid. Can. J. Chem. Eng. 43, 217–223.

Bugg, J., Saad, G., 2002. The velocity field around a Taylor bubble rising in a stagnant viscous fluid: Numerical and experimental results. Int. J. Multiph. Flow 28 (5), 791–803.

Campos, J.B.L.M., Carvalho, J.R.F.G., 1988. An experimental study of the wake of gas slugs rising in liquids. J. Fluid Mech. 196, 27–37.

Cerqueira, R., Paladino, E., 2020. Experimental study of the flow structure around Taylor bubbles in the presence of dispersed bubbles. Int. J. Multiph. Flow 133, 103450.

Cerqueira, R.F., Paladino, E.E., Brito, R.M., Maliska, C.R., Meneghini, C., 2019. Experimental apparatus and flow instrumentation for the investigation of a quasi-real slug flows in vertical ducts. Exp. Therm. Fluid Sci. 102, 421–451.

Cerqueira, R., Paladino, E., Ynumaru, B., Maliska, C., 2018. Image processing techniques for the measurement of two-phase bubbly pipe flows using particle image and tracking velocimetry (PIV/PTV). Chem. Eng. Sci. 189, 1–23.

Collins, R., Moraes, F.F.D., Davidson, J.F., Harrison, D., 1978. The motion of a large gas bubble rising through liquid flowing in a tube. J. Fluid Mech. 89 (3), 497–514.

Čopar, S., Kos, Ž., Emeršič, T., Tkalec, U., 2020. Microfluidic control over topological states in channel-confined nematic flows. Nat. Commun. 11, 59.

Davies, R., Taylor, G., 1950. The mechanics of large bubbles rising through extended liquids and through liquids in tubes. Proc. R. Soc. Lond. A 200, 375–390.

Deen, N., Westerweel, J., Delnoij, E., 2002. Two-phase PIV in bubbly flows: Status and trends. Chem. Eng. Technol. 25, 97.

Dumitrescu, D.T., 1943. Strömung an einer luftblase im senkrechten rohr. Z. Angew. Math. Mech. 23, 139–149.

Ergin, F., Olofsson, J., Petersson, P., Gade-Nielsen, N., 2020. A hybrid phase boundary detection technique for two-phase-flow PIV measurements. Flow Meas. Instrum. 74, 101776.

Fabre, J., Figueroa-Espinoza, B., 2014. Taylor bubble rising in a vertical pipe against laminar or turbulent downward flow: symmetric to asymmetric shape transition. J. Fluid Mech. 755, 485–502.

Ferrari, A., Magnini, M., R., T.J., 2017. A flexible coupled level set and volume of fluid (flexCLV) method to simulate microscale two-phase flow in non-uniform and unstructured meshes. Int. J. Multiph. Flow 91, 276–295.

Fershtman, A., Babin, V., Barnea, D., Shemer, L., 2017. On shapes and motion of an elongated bubble in downward liquid pipe flow. Phys. Fluids 29 (11), 112103.

Frederix, E.M.A., Komen, E.M.J., Tiselj, I., Mikuž, B., 2020. LES of turbulent co-current taylor bubble flow. Flow Turbul. Combust. 105, 471–495.

Frederix, E.M.A., Tajfirooz, S., Hopman, J.A., Fang, J., Merzari, E., Komen, E.M.J., 2023. Two-phase turbulent kinetic energy budget computation in co-current taylor bubble flow. Nucl. Sci. Eng. 197 (10), 2585–2601.

Gui, L., Lindken, R., Merzkirch, W., 1997. Phase-separated PIV measurements of the flow around systems of bubbles rising in water. In: ASME-FEDSM97–3103. ASME.

Hassan, Y., Blanchat, T., Seeley, C., Canaan, R., 1992. Simultaneous velocity measurements of both components of a two-phase flow using particle image velocimetry. Int. J. Multiph. Flow 18 (3), 371–395.

Hassan, Y.A., Ortiz-Villafuerte, J., Schmidl, W.D., 2001. Three-dimensional measurements of single bubble dynamics in a small diameter pipe using stereoscopic particle image velocimetry. Int. J. Multiph. Flow 27 (5), 817–842.

Hassan, Y.A., Schmidl, W., Ortiz-Villafuerte, J., 1998. Investigation of three-dimensional two-phase flow structure in a bubbly pipe flow. Meas. Sci. Technol. 9 (3), 309–326.

Holagh, S.G., Ahmed, W.H., 2024. Critical review of vertical gas-liquid slug flow: An insight to better understand flow hydrodynamics' effect on heat and mass transfer characteristics. Int. J. Heat Mass Transfer 225, 125422.

Holagh, S.G., Ahmed, W.H., 2025. Characterizing the development of gravity-driven slug flows using high-speed imaging and PIV-PLIF techniques. Exp. Therm. Fluid Sci. 160, 111334.

Khalitov, D., Longmire, E., 2002. Simultaneous two-phase PIV by two-parameter phase discrimination. Exp. Fluids 32, 252–268.

Khodaparast, S., Magnini, M., Borhani, N., Thome, J.R., 2015. Dynamics of isolated confined air bubbles in liquid flows through circular microchannels: An experimental and numerical study. Microfluid. Nanofluidics 19, 209–234.

Kren, J., 2024. Dynamics of a Taylor Bubble in Counter-Current Turbulent Flow (Ph.D. thesis). University of Ljubljana, URL: https://repozitorij.uni-lj.si/IzpisGradiva.php?lang=slv&id=161876.

Kren, J., Frederix, E., Tiselj, I., Mikuž, B., 2024. Numerical study of Taylor bubble breakup in counter-current flow using large eddy simulation. Phys. Fluids 36 (2), 023311.

Kren, J., Zajec, B., Tiselj, I., El-Shawish, S., Perne, Ž., Tekavčič, M., Mikuž, B., 2023. Dynamics of Taylor bubble interface in vertical turbulent counter-current flow. Int. J. Multiph. Flow 165, 104482.

LaVision, G., 2024. Davis software. URL: https://www.lavision.de/en/products/davis-software.

Lemmon, E., Bell, I., Huber, M., McLinden, M., 2018. NIST standard reference database 23: Reference fluid thermodynamic and transport properties-REFPROP, version 10.0, national institute of standards and technology. http://dx.doi.org/10.18434/T4/1502528, URL: https://www.nist.gov/srd/refprop.

Lemos, B., de Lima Amaral, R., Bortolin, V., Lemos, M., de Moura, H., de Castro, M., José de Castilho, G., Meneghini, J., 2024. Dynamic mask generation based on peak to correlation energy ratio for light reflection and shadow in PIV images. Measurement 229, 114352.

Liberzon, D., Shemer, L., Barnea, D., 2006. Upward-propagating capillary waves on the surface of short Taylor bubbles. Phys. Fluids 18 (4), 048103.

Lindken, R., Gui, L., Merzkirch, W., 1999. Velocity measurements in multiphase flow by means of particle image velocimetry. Chem. Eng. Technol. 22, 202–206.

Lindken, R., Merzkirch, W., 2000. Velocity measurements of liquid and gaseous phase for a system of bubbles rising in water. Exp. Fluids 29, 194–201.

Lindken, R., Merzkirch, W., 2002. A novel PIV technique for measurements in multiphase flows and its application to two-phase bubbly flows. Exp. Fluids 33, 814–825.

Lu, X., Prosperetti, A., 2006. Axial stability of taylor bubbles. J. Fluid Mech. 568, 173–192.

Magnini, M., Ferrari, A., Thome, J.R., Stone, H.A., 2017. Undulations on the surface of elongated bubbles in confined gas-liquid flows. Phys. Rev. Fluids 2, 084001.

Magnini, M., Herrada, M.A., 2025. Two-dimensional global stability analysis of elongated bubbles moving in a horizontal tube. Phys. Rev. Fluids 10, 053603.

Magnini, M., Khodaparast, S., Matar, O.K., Stone, H.A., Thome, J.R., 2019. Dynamics of long gas bubbles rising in a vertical tube in a cocurrent liquid flow. Phys. Rev. Fluids 4, 023601.
Martin, C.S., 1976. Vertically downward two-phase slug flow. J. Fluids Eng. 98 (4), 715–722.
Mikuž, B., Cerkovnik, K., Tiselj, I., 2024. Asymmetry propagation in a pipe flow downstream of a 90° sharp elbow bend. Appl. Sci. 14 (17).
Morgado, A., Miranda, J., Araújo, J., Campos, J., 2016. Review on vertical gas–liquid slug flow. Int. J. Multiph. Flow 85, 348–368.
Mori, T., Igarashi, R., Hayashi, K., Kurimoto, R., Tomiyama, A., 2024. Surface coverage ratio of contaminated taylor bubbles in a square microchannel. Chem. Eng. Res. Des. 204, 343–353.
Nishino, K., Kato, H., Torii, K., 2000. Stereo imaging for simultaneous measurement of size and velocity of particles in dispersed two-phase flow. Meas. Sci. Technol. 11 (6), 633–645.
Nogueira, S., Riethmuler, M., Campos, J., Pinto, A., 2006a. Flow in the nose region and annular film around a Taylor bubble rising through vertical columns of stagnant and flowing Newtonian liquids. Chem. Eng. Sci. 61 (2), 845–857.
Nogueira, S., Riethmuller, M., Campos, J., Pinto, A., 2006b. Flow patterns in the wake of a Taylor bubble rising through vertical columns of stagnant and flowing Newtonian liquids: An experimental study. Chem. Eng. Sci. 61 (22), 7199–7212.
Nogueira, S., Sousa, R., Pinto, A., Riethmuller, M., Campos, J., 2003. Simultaneous PIV and pulsed shadow technique in slug flow: A solution for optical problems. Exp. Fluids 35, 598–609.
Nop, R., Hamrit, G., Burlot, A., Bois, G., Mikuž, B., Tiselj, I., 2023. The 3D DNS of a Taylor bubble in counter-current flow with a turbulent wake using the Front-Tracking method in TRUST/TrioCFD. In: NENE2023-416. NSS.
Nusselt, W., 1916. Die oberflachenkondensation des waserdampfes. Z. Des Vereines Deutscher Ingenieure 60 (27), 541–546.
Pinto, A., Coelho Pinheiro, M., Nogueira, S., Ferreira, V., Campos, J., 2005. Experimental study on the transition in the velocity of individual Taylor bubbles in vertical upward co-current liquid flow. Chem. Eng. Res. Des. 83 (9), 1103–1110.
Polonsky, S., Shemer, L., Barnea, D., 1999. The relation between the Taylor bubble motion and the velocity field ahead of it. Int. J. Multiph. Flow 25 (6), 957–975.
Saidj, F., Arabi, A., Bouyahiaoui, H., Azzi, A., Hasan, A.H., 2025. Slug void fraction in vertical downward gas–liquid two-phase flow. Phys. Fluids 37 (1), 013367.
Sathe, M., Thaker, I., Strand, T., Joshi, J., 2010. Advanced PIV/LIF and shadowgraphy system to visualize flow structure in two-phase bubbly flows. Chem. Eng. Sci. 65, 2431–2442.
Shemer, L., Gulitski, A., Barnea, D., 2005. Experiments on the turbulent structure and the void fraction distribution in the Taylor bubble wake. Multiph. Sci. Technol. 17, 103–122.
Shemer, L., Gulitski, A., Barnea, D., 2007. On the turbulent structure in the wake of Taylor bubbles rising in vertical pipes. Phys. Fluids 19 (3), 035108.
Shih, Y., Rei, C., Wang, H., 2009. A novel PDE based image restoration: Convection–diffusion equation for image denoising. J. Comput. Appl. Math. 231 (2), 771–779.
Smith, S., Taha, T., Cui, Z., 2002. Enhancing hollow fibre ultrafiltration using slug-flow — a hydrodynamic study. Desalination 146 (1), 69–74.
Sridhar, G., Katz, J., 1995. Drag and lift forces on microscopic bubbles entrained by a vortex. Phys. Fluids 7, 389–399.
Thangam, S., Knight, D., 1989. Effect of stepheight on the separated flow past a backward facing step. Phys. Fluids 1 (3), 604–606.
Tiselj, I., El Shawish, S., Kren, J., Draksler, M., Mikuž, B., 2025. Capillary waves on the liquid film of a Taylor bubble in vertical counter-current flow. Phys. Fluids 37 (7), 073353.
Tiselj, I., Kren, J., Mikuž, B., Nop, R., Burlot, A., Hamrit, G., 2024. Experimental and numerical study of Taylor bubble in counter-current turbulent flow. Arab. J. Sci. Eng..
Tokuhiro, A., Maekawa, M., Iizuka, K., Hishida, K., Maeda, M., 1998. Turbulent flow past a bubble and an ellipsoid using shadow-image and PIV techniques. Int. J. Multiph. Flow 24 (8), 1383–1406.
Tu, Y.-T., et al., 2016. Ray optics simulation. URL: https://phydemo.app/ray-optics.
Van Hout, R., Gulitski, A., Barnea, D., Shemer, L., 2002. Experimental investigation of the velocity field induced by a Taylor bubble rising in stagnant water. Int. J. Multiph. Flow 28 (4), 579–596.
Vassallo, P., Kumar, R., 1997. PIV velocity measurements in the wake of an obstruction simulating a Taylor bubble in a duct. In: ASME-FEDSM97. ASME.
Wallis, G., 1969. One-dimensional Two-phase Flow. McGraw-Hill.
Zhou, G., Prosperetti, A., 2019. Violent expansion of a rising Taylor bubble. Phys. Rev. Fluids 4, 073903.
Zimmer, M.D., Bolotnov, I.A., 2019. Slug-to-churn vertical two-phase flow regime transition study using an interface tracking approach. Int. J. Multiph. Flow 115, 196–206.
Zimmer, M.D., Bolotnov, I.A., 2020. Exploring two-phase flow regime transition mechanisms using high-resolution virtual experiments. Nucl. Sci. Eng. 194 (8–9), 708–720.
Zimmer, M.D., Bolotnov, I.A., 2021. Evaluation of length scales and meshing requirements for resolving two-phase flow regime transitions using the level set method. J. Fluids Eng. 143 (6), 061403.
Zukoski, E.E., 1966. Influence of viscosity, surface tension, and inclination angle on motion of long bubbles in closed tubes. J. Fluid Mech. 25 (4), 821–837.